Thermal transport measurements in 1.05 μm laser irradiation of spherical targets

B. Yaakobi, J. Delettrez, L. M. Goldman, R. L. McCrory, R. Marjoribanks, M. C. Richardson, D. Shvarts,[a] S. Skupsky, J. M. Soures, C. Verdon, D. M. Villeneuve, T. Boehly, R. Hutchinson, and S. Letzring

Laboratory for Laser Energetics, University of Rochester, 250 East River Road, Rochester, New York 14623

Transport and implosion experiments have been conducted on the OMEGA 24-beam, uniform-irradiation facility. Thermal transport in spherical irradiation was found to be different than in comparable, single-beam target irradiation and could not be described in terms of a flux-inhibited model. Deep energy deposition in spherical irradiation (by electrons on the tail of the thermal velocity distribution) was found to lead to a temperature profile which is not as steep as predicted by a flux-inhibited model. This apparently leads to more explosive implosion (i.e., higher core temperature) than predicted by using such a model.

I. INTRODUCTION

Thermal transport is one of the crucial parameters affecting target performance in laser fusion. Higher thermal conduction results in better target performance, i.e., higher ablation pressure and higher hydrodynamic efficiency. Simply stated, higher thermal conduction means that more of the target mass is heated (to a lower temperature). Since for a given energy the momentum is higher for lower velocity, this corresponds to a higher ablation pressure. Also, ablating more mass directly translates to a higher hydrodynamic efficiency.[1] Many experiments to determine transport have been conducted in single-beam irradiation geometry. In recent spherical irradiation experiments[2] less inhibited transport was claimed than most single-beam experiments[3-6] have shown (flux limiter of 0.1 as compared with 0.03–0.05). Plane-target irradiation experiments typically showed inhibition described by $f \lesssim 0.65$ at a variety of laser wavelengths. The flux limiter f is defined by the condition that the heat flux is not allowed to exceed the quantity $f n_e k T_e (k t_e / m_e)^{1/2}$ where n_e, T_e, and m_e are the electron density, temperature, and mass, respectively. We have undertaken a systematic study of transport in spherical geometry using the OMEGA 24-beam, uniform irradiation facility at $\lambda = 1.05 \mu m$ with $f/3$ optics. Experiments were done with 2 kJ, 1 nsec pulses at irradiances of 5×10^{13}–10^{15} W/cm^2. We found that the experimental results could not be adequately modeled with flux-limited transport for any f value—not even uninhibited $(f = 0.65)$, or classical, transport. The unique features of these experiments with respect to most previous experiments are as follows.

First, a high degree of spherical symmetry of the irradiation geometry. This minimizes the contribution of lateral heat transport and, therefore, enables us to study the radial (inwards) heat transport with less confusion. Second, the relatively high laser energy permits one to work with larger targets for a given irradiance. This leads to longer scale

lengths and a much smaller contribution of resonance absorption to the overall absorption. Thus, thermal transport is much less clouded by the issue of transport by suprathermal electrons.

The burnthrough depth in parylene (CH), as determined by the signature of x-ray lines from an aluminum substrate, was found to be about three times higher than predicted by a flux-limited model, for a laser irradiance in the range 5×10^{13}–1×10^{15} W/cm^2. However, in single-beam irradiation of spheres, with a focal spot diameter of 70–150 μm, the burnthrough depth was about that predicted by a flux-limited model. This apparent agreement with theory is approximately true for spherical irradiation where higher energy lines are used as burnthrough signatures (Ti, Ni). Streaked x-ray spectra (using filters) and x-ray microscope images do not support evidence of penetration at only isolated locations due to hot spots. The low level of K_α-line emission from the substrate is consistent with a deeper penetration of the leading edge of the temperature profile, as indicated by the burnthrough measurements, as is the high density measured by dielectronic satellite lines of Al.

The effect of a modified description of transport on target implosion was studied. The implosion was found to be more explosive than predicted by an uninhibited transport simulation—core temperatures in the experiment were higher but densities were lower. It also appears that preheat in spherical targets at irradiances below $\sim 10^{15}$ W/cm^2 may not be determined by suprathermal electrons but by the properties of the thermal front discussed here, which appears to have a weaker dependence on the irradiance.

II. TRANSPORT DETERMINATION BY BURNTHROUGH MEASUREMENTS

Thermal transport can be deduced in a simple and accurate way[3] by measuring the intensity of appropriate x-ray lines from a substrate layer as a function of the overcoat layer thickness ("burnthrough" measurements), and then comparing with code predictions. A high degree of uniformity is essential when comparing experimental transport results to a one-dimensional code (the laser absorption is treated with a

[a] Visiting scientist on leave from the Nuclear Research Center, Negev, Israel.
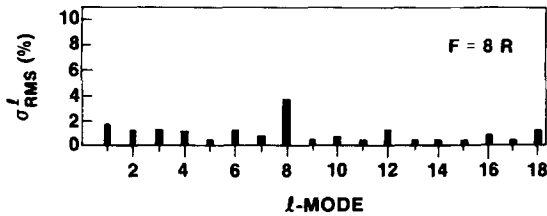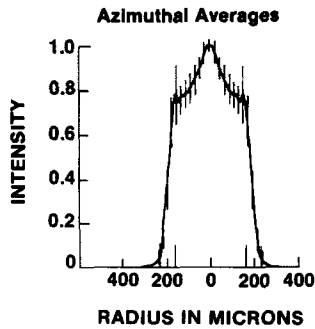
Azimuthal Averages

FIG. 1. The calculated uniformity of spherical irradiation achieved in these experiments, based on the measured beam profiles. In (a) is shown an azimuthally averaged on-target profile distribution of one of the 24 beams. Two long bars on both sides of $R = 0$ encompass 50% and 90% of total energy. The error bars indicate variation over the azimuthal angle. The absorbed energy distribution is decomposed into spherical harmonic modes (b). Adding them up results in a total rms modulation of 6%. The beams are assumed to be focused eight radii behind the target center.

ray-tracing procedure and is therefore two dimensional). Uniform irradiation is obtained by focusing at a point which is about eight target radii behind the target center. *The resulting nonuniformity of the overlapping 24 beams has a rms intensity variation smaller than 6%.* We show in Fig. 1 the calculated uniformity of spherical irradiation achieved in these experiments, based on the measured beam profiles.

Figure 1(a) shows a typical, radially averaged beam profile. The uniformity calculation uses this average profile and the actual energies of the 24 individual beams, which vary between them by less than 5%. Using a ray-tracing proce-

dure, the absorption due to inverse bremsstrahlung of this irradiation distribution is then calculated; the absorbed energy distribution is decomposed into spherical harmonic modes, the distribution of which is shown in Fig. 1(b). Adding up the various spherical harmonic modes results in 6% rms of absorbed intensity modulation.

The targets used in this study were thin glass shells of diameter approximately 400 μm, coated with a 2 μm thick copper layer. The copper coating made the target massive enough, hence immobile, so that the transport issue would not be complicated by hydrodynamic motion. The copper layer was coated with a "substrate layer" which provided signature x-ray emission, measured with x-ray Bragg spectrographs and spectrally resolving x-ray streak cameras. The substrate layer was finally overcoated with varying thicknesses of ablator material. The thickness and uniformity of the ablator layer (parylene) are the most pertinent parameters in the transport experiments: the precision of controlling the parylene deposition thickness was $\pm 0.1 \mu$m (for any thickness layer); optical interferometric tests showed nonconcentricity, or large-scale nonuniformity of less than 5% of parylene layer thickness. Table I summarizes the parameters in these experiments. The x-ray diffraction crystals and films were absolutely calibrated.[7] In the following figures, we show sample data which refer to a single x-ray line (intensity integrated over the line profile); the comparison of curves for different spectral lines from the same spectrum is of secondary importance to the questions at hand.
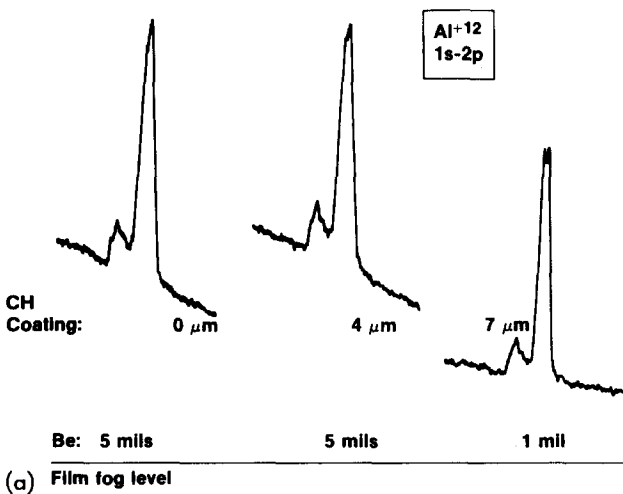
The results were compared to those calculated by the one-dimensional, Lagrangian, laser fusion code LILAC.[8] This is a two-fluid code (electron and ions) that includes hydrodynamic motion together with energy transport from thermal conductivity, shocks, suprathermal electrons, and radiation. Suprathermal electrons from the laser–target interaction were transported with 20 energy groups. Radiation was transported in 50 frequency groups using opacity tables[8] developed at the Los Alamos National Laboratory. The Thomas–Fermi equation of state was used throughout. Rate equations were used to calculate x-ray line intensities (accounting

TABLE I. Parameters in transport experiments. Pulse width is 1 nsec, targets are glass shells of thickness ~1 μm, coated with 2 μm of copper, then with a substrate and coating layers. Values are averages over a series of experiments, with typically $\pm$ 10% variation. For tangential focusing the $f/3$ optics is adjusted to focus at 8 radii behind the center of the target. Bracketed numbers are thicknesses in microns.
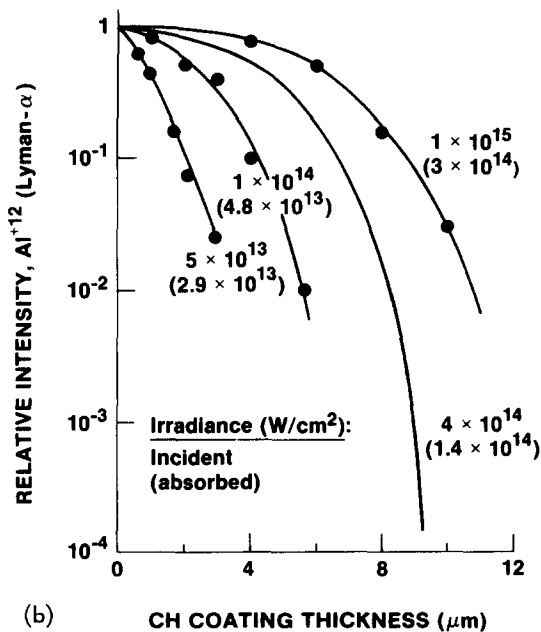
No.	No. of beams	Irradiance W/cm^2	Laser energy (kJ)	Focusing	Target dimensions (m)		Coating	Figure
					Diameter	Substrate		
1	24	5×10^{13}	0.3	tangential	400			2
		10^{14}	0.6	tangential	400	Al	CH	2
		4×10^{14}	1.9	tangential	400	(1)	(0-12)	2
		10^{15}	1.8	tangential	200			2
2	24	4×10^{14}	0.48	70 μm spot	400	Al	CH	6
	1	4×10^{14}	0.08	150 μm spot	400	(1)	(0-4)	6
3	24	4×10^{14}	1.8	tangential	400	Al	Ti	5
						(1)	(0-2)	
4	24	4×10^{14}	2.0	tangential	400	Ti(1.5)	CH	7, 9
						Ni(0.5)	(0-8)	7, 10
5	24	10^{15}	1.9	tangential	200	Ti(1.5)	CH	...
						Ni(0.5)	(0-8)	8

also for radiation transport, i.e., opacity); however, we find by inspecting code results that a simple description in terms of the excursion of temperature contours can be adequate for a comparison with the experiment. The absorption is calculated by ray-tracing the incident beams and including inverse bremsstrahlung and resonance absorption. The latter is calculated by an equation describing the tunneling to the critical layer[9] for various ray-traced beams. The only adjustable parameter of relevance here is the flux limiter. The laser energy which reaches the critical layer is converted in the code to suprathermal electrons (this is typically 10%–15% of the energy reaching the turning point).

Figure 2 shows sample spectra and burnthrough curves for various incident (and absorbed) irradiances. Here the intensity of the $2p$-$1s$ line of Al^{+12} at 1.73 keV is plotted against the thickness of the parylene coating thickness. The intensity of the dielectronic satellites adjacent to this line [see Fig. 2(a)] were not included; they are much weaker than the resonance line for any thickness. For each of these cases, the "penetration depth" is about three times larger than what is predicted by LILAC for a flux limiter ($f = 0.03$–0.05), and it is comparable to what is predicted for no flux limitation ($f = 0.65$). The thermal energy required to heat the amount of material corresponding to the measured penetration depth is still only about 5% of the absorbed laser energy. The fact that we do not observe any threshold for this departure from theory suggests that it is not caused by hot spots which would lead to nonuniform heat penetration. This conclusion is supported by x-ray streak camera measurements (Fig. 3) which show that the sharp rise in intensity (due to penetration into the substrate) occurs progressively later in time for thicker parylene thicknesses. This is consistent with an orderly and uniform penetration into the target. This is particularly borne out by the sharp intensity rise due to penetrating the substrate. To explain the results by penetration due to hot spots, we would have to assume nine times higher irradiance within the hot spots as compared to the average irradiance. This is because the measured penetration is about three times deeper than predicted and the penetration depth is about proportional to the square root of the irradiance [see Fig. 2(b)]. However, experiments with such "spotty" irradiance (Fig. 6 below) shows that the penetration is actually much smaller than with uniform irradiation. This conclusion is additionally supported by x-ray microscope images shown in Fig. 4 for various parylene thicknesses. Uniform heat-front progres-
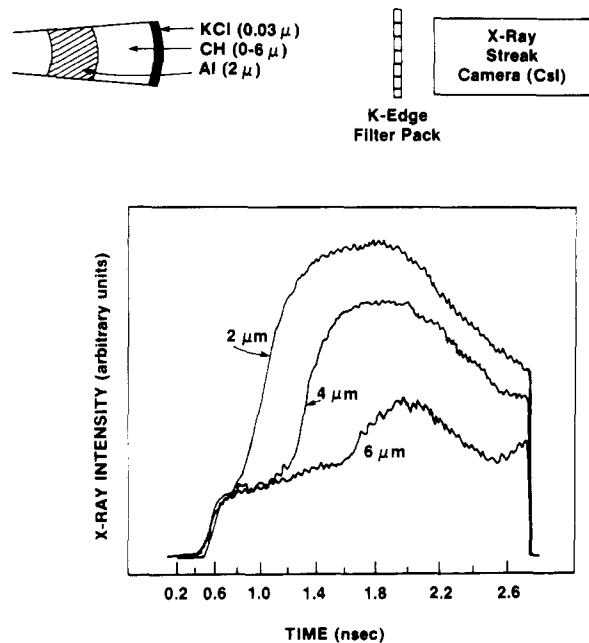

FIG. 2. (a) Examples of the measured Lyman-α line of Si^{+13} (and its nearby satellites). The three spectra have the same film density units and the same film fog level. However, the total thickness of the beryllium window and attenuator (marked below the spectra) is different. Measuring simultaneously through several attenuators greatly increases the dynamic range. (b) The burnthrough of parylene (CH) into aluminum in spherical irradiation. The curve for $I = 4 \times 10^{14}$ W/cm^2 is from Fig. 6.

FIG. 3 The x-ray streak traces as a function of CH coating thickness. Irradiance: $I = 4 \times 10^{14}$ W/cm^2. Saran filter (containing chlorine) in front of the camera selects the photon energy range ~ 1.5–2.5 keV, which includes the aluminum line used in Fig. 2(b). The first rise in intensity (at 0.5 nsec) marks the heating of the KCl surface layer. The second rise is due to the penetration into the aluminum substrate. The peak of the laser pulse occurs at about 1.6 nsec.
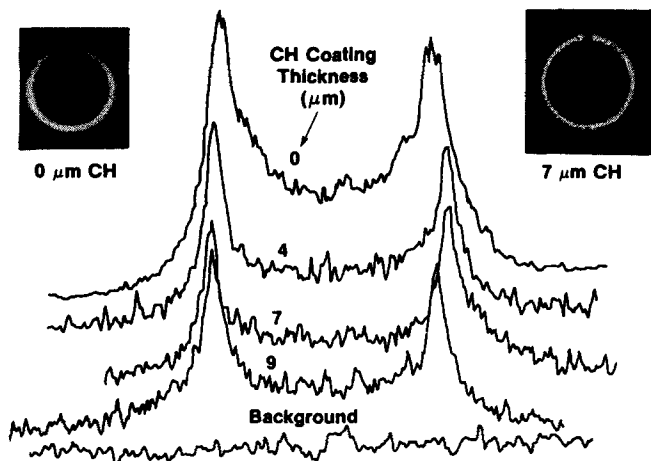
FIG. 4. Radial densitometer traces through the two-dimensional x-ray microscope images (rings) of targets in Fig. 2 at $I = 4 \times 10^{14}$ W/cm^2. The dense ring position corresponds to the initial target diameter. The film calibration has not been folded into these raw data. The insets show two examples of the original imaging data; the image of the uncoated target was filtered much more heavily than the second image.

sion is strongly suggested by the "limb-darkened" profiles as well as by the fact that the intensity fluctuations in the center of the image (especially for the thickest coating) can be totally accounted for by film noise. Filamentations could generate or aggravate nonuniformities of energy deposition; because of the long irradiation wavelength and low target Z, they would be due to ponderomotive rather than thermal self-focusing. However, they exist only in the underdense plasma. Therefore, for transport studies one should emphasize signatures such as x rays, which probe the supercritical density regions.

A few remarks on the streak results of Fig. 3 are in order. The question arises as to why the emission from the fiducial KCl layer does not decay after its ablation. One reason is that with bigger targets the expansion cooling is slower. Moreover, the sensitivity curve of the setup (photocathode plus filter) excludes the strong K and Cl lines but includes the recombination continuum; this feature is favored by a falling temperature. The results for the various energy channels in the range of approximately 1.5–4 keV are similar to those of Fig. 3. However, due primarily to a lower sensitivity of the streak camera, results for higher photon energies (5–8 keV) were not obtained and could not be compared with the results obtained below for x-ray line energies in this range (Ti and Ni substrates). By integrating the curves of Fig. 3 over time, we obtain burnthrough curves which are similar but not identical to those of Fig. 2. The streak camera–filter combination, within a given channel, integrates over several lines as well as the underlying continuum. Since the opacity is then much smaller than for a resonance line (such as in Fig. 2), the obtained burnthrough curves then drop gradually rather than having a flat top. Additionally, the streak camera measurements have a smaller dynamic range than the time-integrated data.

To determine that the enhanced penetration is not dependent on the choice of coating material, we performed similar experiments on titanium coatings over aluminum. In
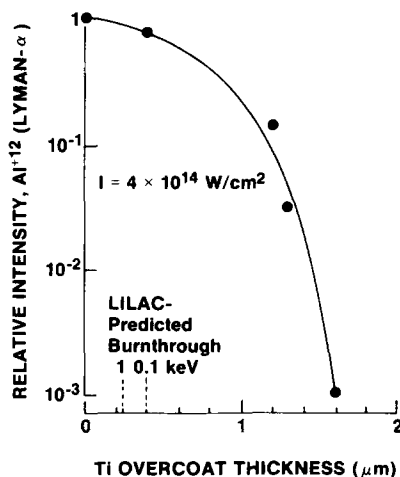

FIG. 5. Burnthrough of titanium into aluminum. The LILAC-predicted burnthrough depths are for a flux limiter of $f = 0.03$

Fig. 5 we compare the results with the penetration depth predicted by LILAC (which includes a multigroup diffusion treatment or S_n transport treatment[8] of the radiation). A disagreement with a flux-limited model, as was found with parylene coated targets, is evident. Also, the computed penetration depths relative to two temperature values (0.1 and 1 keV) are seen in Fig. 5 to be almost identical; this means that the concluded disagreement with the experiment does not depend on the particular definition of penetration depth we choose. This is an indication of a steep calculated temperature profile at the heat front.

It should be pointed out that in code simulations for this and all other transport shots, the maximum heat-front penetration always occurs at about 1–1.2 nsec after the peak of the pulse. This is in general agreement with the time-resolved spectral measurements (Fig. 3). The case of titanium-coated targets is different than the case of CH coating since x-ray radiation by the titanium contributes significantly to heat transport. The code treatment of radiation diffusion is adequate as evidenced by the fact that the predicted x-ray intensity of the continuum around 1 keV (in this and other experiments) agrees very well with the experiment. Strong isolated spectral lines are not adequately described by a radiation diffusion model, but their contribution to heat transport is small.

Since the present results for uniform, spherical irradiation are markedly different than most reported results for single-beam, plane-target irradiation,[2,4–6] we compared uniform and nonuniform irradiation of spherical targets at the same incident irradiance (see Fig. 6). For comparison with nonuniform irradiation, we conducted experiments in two additional geometries: (a) one single beam (of the OMEGA 24 beams) was focused to a 150 μm spot size on spherical targets, and (b) all 24 beams were focused to small discrete spots, of diameter 70μm, on the surfaces of spherical targets. The incident irradiance in all these cases was adjusted to the same approximate value: 4×10^{14} W/cm^2. The nonuniform irradiance curve in Fig. 6 agrees with a code prediction assuming $f = 0.03$ and spherical symmetry. We are led to conclude that this agreement is fortuitous: some two-dimension-
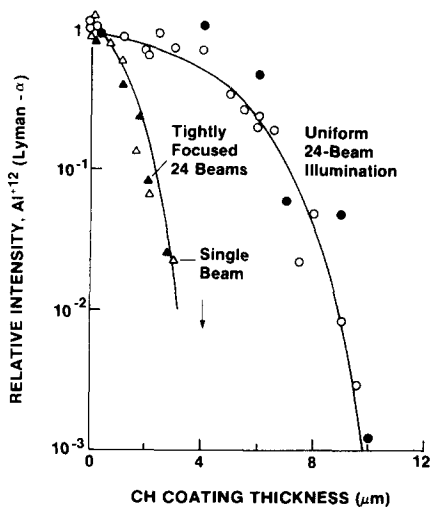
FIG. 6. Comparison of burnthrough (parylene over aluminum) in uniform and nonuniform irradiation of spherical targets, all at approximately the same incident irradiance, 4×10^{14} W/cm^2. The arrow indicates points below the threshold for detectability. The two curves were separately normalized to 1. The full and empty circles pertain to two separate series of experiments.

FIG. 7. Burnthrough of parylene coating into various substrate materials. For aluminum substrates the x-ray line whose intensity is plotted is the Lyman-α line of Al^{+12} (curves from Fig. 6); for titanium and nickel substrates it is the 2^1P-1^1S resonance line of the helium-like ion (Ti^{+20} at 4.75 keV, Ni^{+26} at 7.8 keV). Incident irradiance: 4×10^{14} W/cm^2.

al effects apparently manifest themselves as an effective flux inhibition.

Since the flux inhibition concept was first introduced by Malone, McCrory, and Morse,[4] a theoretical substantiation has been produced.[10,11] Simply stated, for sharp gradients such as predicted for irradiances of interest to laser fusion, the bulk of the distribution of electron velocities makes little contribution to the transport (the slower particles have a *negative* contribution to the heat flux because of the retarding electric field). Inhibition is a natural result of the fact that only a small fraction of the electrons (i.e., those whose velocity is two to three times the thermal velocity) contribute materially to the transport. However, the long mean free path of those electrons which do contribute to the transport results in nonlocal deposition of heat which affects heat deposition in an opposite sense to that of inhibition.

Mapping of the heat-front temperature profile is essential to the understanding of transport in spherical geometry. We have extended the burnthrough measurements to plastic-coated targets with titanium and nickel substrates. Figures 7 and 8 summarize the results for incident irradiances of 4×10^{14} and 10^{15} W/cm^2, respectively. The aluminum line at 1.73 keV probes temperature contours near 400 eV, while the corresponding titanium line at 4.75 keV and the nickel line at 7.8 keV probe higher temperatures, near approximately 1 keV and approximately 1.5 keV, respectively. The marked difference between the low-Z and high-Z burnthrough curves is evidence of a very gradual temperature fall at the heat front. It shows the inapplicability of the flux-limited model (with any f) for which these curves are predicted to almost coincide (see Fig. 5). We can speak of a penetration of only a "foot" of relatively low temperature ahead of the heat front into the higher density, deeper target layers. The rest of the heat front can still be described by flux-inhibited transport.

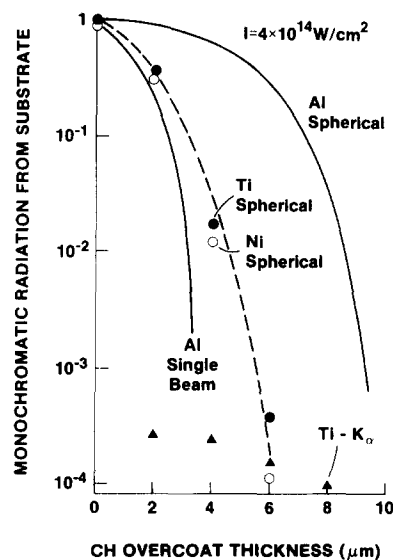Increased heat penetration in the target (with respect to

the predictions of the flux-limited model) results in lower calculated corona temperatures and, hence, higher calculated values of inverse-bremsstrahlung laser absorption. Because this increased penetration does not seem to apply to the high-temperature contours (Figs. 7 and 8), the effect on calculated laser absorption is smaller than it would be for uninhibited-flux calculations. This is consistent with $2\omega_p$ imaging of the target which indicates that the excursion of the critical layer is consistent with inhibited transport ($f \sim 0.03$). For less inhibited transport, the outward mass flow should have increased, resulting in a farther excursion of the critical layer. Thus, except for a deep penetration of
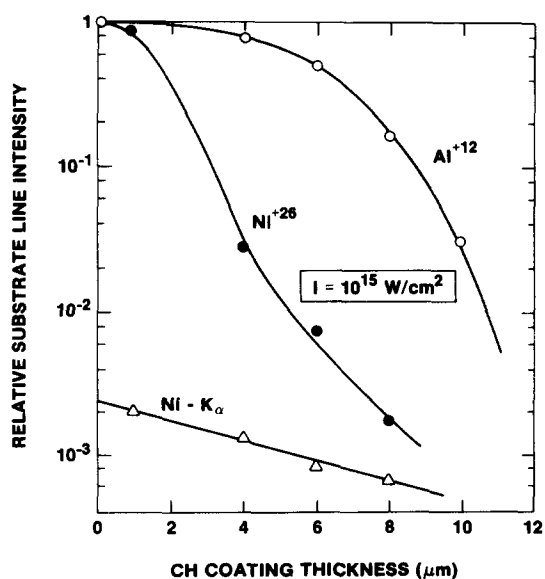

FIG. 8. Similar curves to those in Fig. 7 but for an incident irradiance of 10^{15} W/cm^2.

relatively low temperature contours, the rest of the interaction region seems to behave as in a flux-inhibited model.

III. PREHEAT DETERMINATION USING K_α LINES

Figures 7 and 8 also illustrate the intensity of K_α lines from the high-Z substrate which are indicative of preheat by fast electrons. Using the intensity of the (unshifted) K_α lines in absolute magnitude, we estimate[12] that only about 0.3% of the absorbed energy at 4×10^{14} W/cm^2 is deposited as fast electron preheat. For an irradiance of 10^{15} W/cm^2 the preheat fraction is approximately 0.7%. Electron preheat has been shown to be relatively small even at a higher irradiance, as one goes to longer laser pulses.[5] However, the relative intensity of K_α radiation here is much lower than predicted[9] and lower than in comparable plane target experiments.[12] The LILAC code prediction for the fraction of the absorbed energy which appears as preheat is 9% at 5×10^{13} W/cm^2, 11% at 10^{14} W/cm^2, 12% at 4×10^{14} W/cm^2, and 14% at 10^{15} W/cm^2. This fraction increases slowly with irradiance partly because at a higher irradiance a larger fraction of the fast electrons' energy is converted to accelerated ion energy. Measurements of the continuum x-ray spectrum on plastic sphere targets confirm a relatively low temperature (rising from 2 to 5 keV for 5×10^{13} to 10^{15} W/cm^2) of resonance absorption electrons. Because of this low value, it is difficult to determine the fractional energy imparted to them but it is higher than 10%. It is thus seen that the observed K_α lines cannot account for the amount of preheat predicted by theory. In fact, the code-calculated K_α intensity at the various irradiance values is about a factor 10 higher than measured. We will contend below that since the heat front drops gradually into the target, the fast electrons generated at the critical layer deposit most of their energy in a relatively high temperature layer ahead of the critical layer. In this case, cold K_α lines cannot be produced. However, we will then have to also consider shifted K_α lines which are emitted by partly ionized atoms. Figure 9 shows the spectra of Ti^{+20} line radiation and the nearby K_α radiation for various parylene coating thicknesses; Fig. 10 shows similar spectra for a nickel substrate. All the transport targets in these experiments were made from copper-coated glass shells, where fast electrons can penetrate through the thin, 0.5 μm nickel layer and excite Cu K_α radiation. For no parylene ablator coating, the same is true for the heat front itself (upper curve, Fig. 10). Both Figs. 9 and 10 correspond to an irradiance of 4×10^{14} W/cm^2. Only unfiltered spectra are shown, where the weak K_α lines can be seen; the intensity of the high ionization lines for thin CH coatings, which saturate the film, was determined from heavily filtered spectra taken simultaneously.

Using a simple model, we can deduce the fast electron temperature from the measured K_α line attenuation with increasing CH coating thickness. Assuming a hot-electron Maxwellian distribution of temperature T_H, we calculate for each group its energy after attenuation through a given CH thickness; we then multiply by the cross section to eject a K-shell electron in the substrate atom at that energy, and finally integrate over all energies above the K edge. The result is proportional to the K_α intensity.[12] The resulting curves
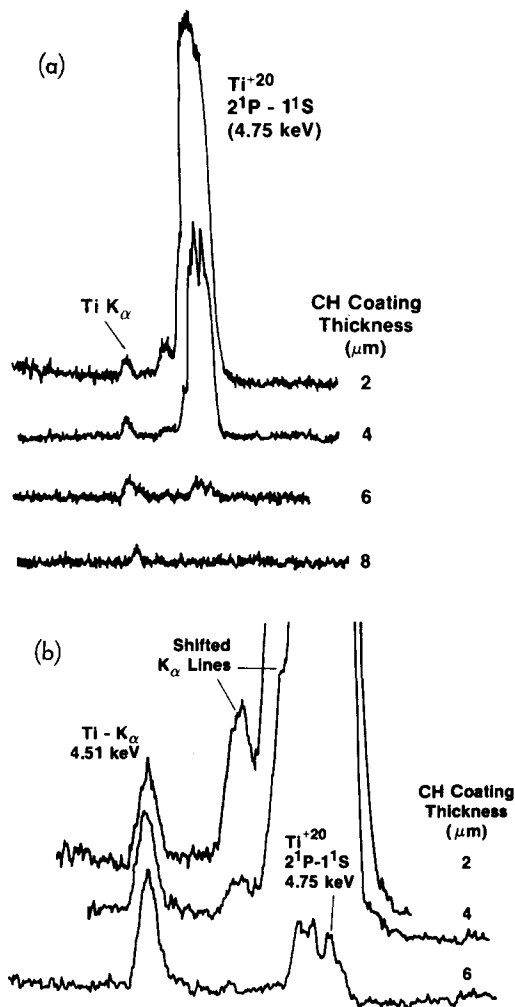

FIG. 9. (a) Titanium spectra at $I = 4\times10^{14}$ W/cm^2. Photon energy increases to the right. (b) Same spectra on an expanded scale, showing shifted K_α lines, some of which are marginally resolved from the Ti^{+20} feature. Due to a difference in background level, the actual line intensities fall faster with CH thickness than seems in these plots of raw data. Titanium layer thickness: 1.5 μm.
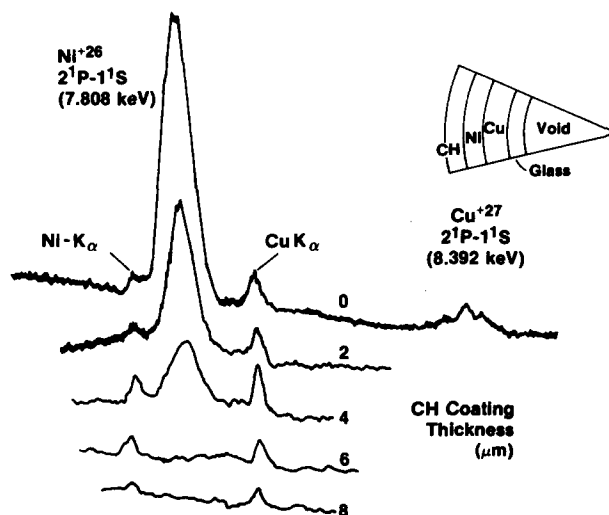

FIG. 10. Nickel (and copper) spectra at $I = 4\times10^{14}$ W/cm^2. The densitometer sensitivity used was higher for thicker CH coatings. Photon energy increases to the right. Layer thicknesses: glass, 1 μm; copper, 2μm; and nickel, 0.5 μm.
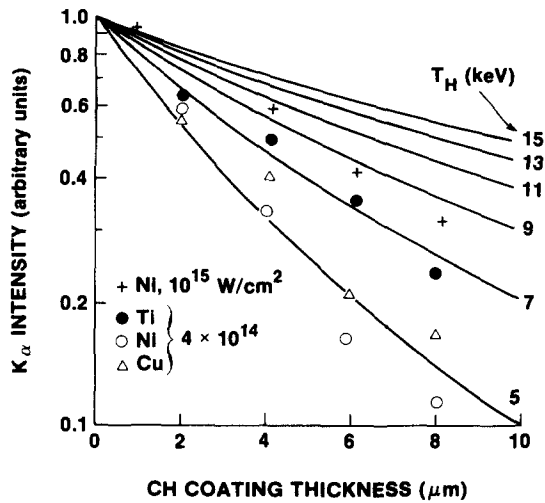
FIG. 11. Measured and model-calculated K_α line intensity assumed to be excited by fast electrons of temperature T_H.

(Fig.11) show a slower drop with increasing plastic thickness, because of the preferential attenuation of the slower electrons. The deduced T_H values: 5–7 keV at 4×10^{14} W/cm^2 and approximately 9 keV at 10^{15} W/cm^2 are in good agreement with theoretical predictions[9] for electrons generated by resonance absorption. The electron attenuation (and preheat) refers to the plastic coating and the high-Z substrate serves only as a probe in this analysis. Therefore, the extrapolation of the K_α intensity to zero CH thickness (in Fig. 11) yields the K_α intensity to be used for the preheat estimate.

Because radiative preheat in plastic is small, it is neglected in this analysis. If the observed K_α lines were excited by radiation they would imply a much lower level of preheat than estimated here.[9] A simple estimate shows that the deduced preheat energy deposited along a depth indicated by Figs. 9–11 is much too small to give rise to Al^{+12} (or Al^{+11}) emission. Alternatively stated, suprathermal electrons, by themselves, cannot account for the observed burnthrough. However, resonance-absorption electrons which move inwards from the critical layer encounter a layer of thickness of the order of their range (see Figs. 7, 8, and 11) which is already heated by the penetrating "foot" of the heat front. Therefore, the emission of K_α radiation which requires cold material is reduced. However, as we shall see below, this "foot" itself constitutes preheat. Resonance-absorption electron temperature depends on the irradiance approximately like $I^{0.5}$ and on the electron range like I. However, Fig. 2 indicates penetration due to this thermal "foot" which depends on I only like $I^{0.5}$. It appears, therefore, that lowering the laser irradiance may have less of a beneficial effect, in terms of avoiding preheat, than previously thought.

Additional supporting evidence for this preheating mechanism can be obtained from shifted K_α lines.[12] Figure 9(b) shows an additional spectral feature between the Ti K_α line and the Ti^{+20} group of lines. This is due to K_α emission in titanium ionized 16–18 times. Additionally, higher ionization shifted K_α lines are marginally resolved from the Ti^{+20} feature. Since the ionization energy of these ions lies in the range 1.1–1.3 keV, their existence indicates a region of tem-

perature 300–500 eV. This is evidence of the low-temperature region ahead of the heat front, which can give rise to Al^{+11} lines but not to Ti^{+20} lines. For a thin CH coating, that feature is more intense than the K_α line, indicating that this region extends over a sizable fraction of the suprathermal electron range. However, the faster reduction in intensity of that feature with CH thickness, as compared with that of K_α, indicates preheat other than that caused by suprathermal electrons. In Fig. 10, comparable spectral features apparently merge and broaden the Ni^{+26} group of lines. If we include shifted K_α lines in the analysis described above, the measured preheat energy approaches, but still does not agree with predicted values. This can be an additional indication of a very gradual temperature drop from the critical layer into the target.

It has been suggested[2] that soft x-ray radiation below the carbon K edge may contribute to heating the substrate and thus explain the observations without evoking electron heat transport. We can show this not to be the case. The LILAC-calculated total x-ray emission for the experimental conditions of, say, Fig. 7 amounts to about 3% of the absorbed energy. We use this value in the following estimate, noting that measured x-ray emission data[13] agrees well with this value. About one-eighth of this x-ray flux is emitted within the transmission window below the carbon K edge (from about 0.18 to 0.283 keV); it is transmitted with little attenuation through the parylene layer and heats the substrate directly. The flux between 0.283 keV and about 1 keV is strongly absorbed by a few micron thickness of parylene and cannot affect the substrate temperature. The flux above about 1 keV is also deposited mainly in the substrate, but the amount of energy in this part of the spectrum is much smaller than one-eighth the total flux. The flux within that transmission window for the conditions of Fig. 7 amounts to about 3 J/nsec. The substrate temperature will be determined mainly by the radiation losses, which for the solid density, deep target layers will be governed by Planck's blackbody equations. The temperature at which such losses exactly balance out a 3 J/nsec deposition rate is $T = 50$ eV. This mechanism is thus not negligible but it cannot account for the observed Al^{+12} line emission. We finally note that the delayed substrate emission (see Fig. 3 and the relevant discussion) is also inconsistent with the possibility of significant substrate heating by x-ray radiation from the parylene coating.

IV. MASS ABLATION RATE

Burnthrough curves [see Fig. 2(b)] can be used to obtain the peak mass ablation rate. The total mass ablated is taken as that corresponding to the maximum penetration of the aluminum emission curves in Fig. 2(b) (defined here as the coating thickness where the intensity of the measured substrate x-ray line drops by a factor of 100 from the bare substrate value). After dividing by the pulse width and applying a small correction factor[14] we arrive at the results shown in Fig. 12(a). The area used here is that of the original target; for these nonimploding targets this is very nearly the same as that of the ablation surface.
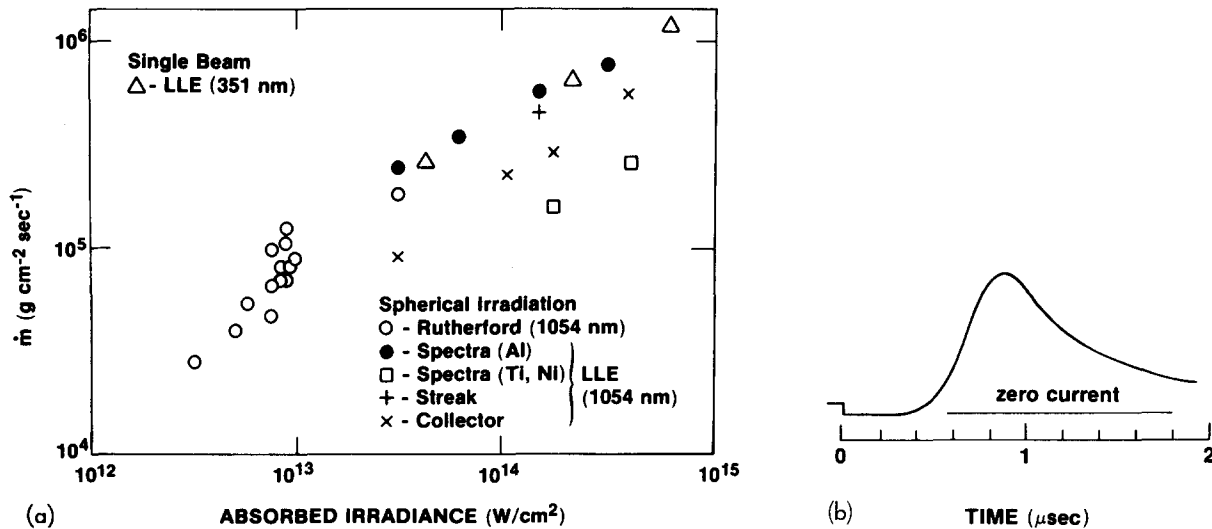
FIG. 12. (a) Comparison of mass ablation rates as a function of absorbed irradiance. Results marked by solid circles were obtained from the burnthrough curves in Fig. 2(b); by square, from the results in Figs. 7 and 8; by crosses, from streak traces, Fig. 3; and by ×'s, from charge collector signals. (b) A typical charge collector current, at a distance of 75 cm from the target.

The streak camera results (Fig. 3) lead directly to the mass ablation rate by taking the time difference of the onset of the second rise in successive traces. For example, for the 2 and 4 μm coating thicknesses, this onset in Fig. 3 occurs near 0.8 and 1.2 nsec, respectively.

The mass ablation rate can be alternatively determined from the average ion velocity as measured by charge collectors [Fig. 12(b)]. If E_a is the absorbed energy per unit area, V the ion expansion velocity, and Δt the pulse width, the mass ablation rate is given approximately by $\dot{m} = 2E_a/V^2\Delta t$, where V^2 is averaged over the distribution. The mass ablation rate so derived (corrected as above[14]) is shown in Fig. 12(a) to be consistently lower than that derived spectroscopically. This indicates that the deep penetration of lower temperature contours does not contribute to drive efficiency as much as if the entire heat front had penetrated to the same depth. This is qualitatively in agreement with calculations employing a nonlocal heat transport (see below) which show deep penetration of the low-temperature part of the heat front. This penetration heats up target layers which move inwards and are not ablated throughout the laser pulse. The higher difference between the two methods at lower irradiance could be due to a higher fraction of neutrals among the expanding plasma, which are not detected by the charge collector.

For comparison, we show results[2] obtained at the Rutherford Laboratory using spherical irradiation at $\lambda = 1.05$ μm and results reported by us previously,[3] using a single beam irradiation at $\lambda = 0.35$ μm.

A few important conclusions can be drawn from these comparisons.

(a) By extending previous spherical irradation data to higher irradiances, we find that the sharp $I^{0.86}$ increase of $\dot{m}$ turns into a weaker $I^{0.5}$ dependence at higher I values.

(b) We find approximately the same slope for the curves of $\dot{m}$ as a function I for spherical (1.05 μm) and flat (0.35 μm) target geometries [see Fig. 12(a)]. The sharp difference

between these two cases in Ref. 2 can be attributed to (i) a simple extrapolation of the spherical data to higher I values, which Fig. 12(a) shows to be inadequate, and (ii) the smaller focal spot in the plane target irradiation at Rutherford, where strong lateral heat conduction apparently clouds the issues at hand (see below).

(c) Since $\dot{m}$ in spherical irradiation was found[2] to be about the same at different laser wavelengths (for the same *absorbed* irradiance) we can speculate from Fig. 12(a) that for $\lambda = 0.35\mu$m, $\dot{m}$ would be about the same for single beam and for uniform irradiation. This contrasts with our finding for 1.05 μm irradiation that $\dot{m}$ for uniform irradiation is about *three times higher* than most reported results for the single-beam case. In the Rutherford experiments, $\dot{m}$ from the charge collector is only 20% lower than $\dot{m}$ from the spectroscopic results. The reason for this difference with the results reported here is not well understood.

These observations provide an improved understanding of transport. Nonlocal heating using a multigroup model for transport results in a more gradual temperature drop into the target,[11,15] which is consistent with the results of Fig. 7. This "smearing" of the heat front results from the longer mean free path of electrons in the tail of the thermal electron velocity distribution. We expect these effects to diminish in importance as we go to shorter-wavelength irradiation because of the increase in density (and, in addition, a *decrease* in temperature if we compare different wavelengths at the same absorbed irradiance).

In order to fully understand the impact of the multienergy group nature of transport one needs to incorporate the equivalent of Fokker–Planck treatment[11] into a hydrodynamic code. This has been done using an approximation (a "hybrid" treatment) which greatly economizes computation time while preserving the essential multigroup, nonlocal character of transport.[16] Preliminary results obtained with this hybrid model incorporated into LILAC indeed show a more gradual temperature fall, consistent with Fig. 7. How-

ever, it seems that the experiment shows a bigger effect of penetration than calculated by this hybrid model. Employing the hybrid model for a quantitative analysis of these experiments is currently underway and will be described elsewhere. Additionally, this model results in a much steeper temperature fall when the laser wavelength is changed from 1.05 to 0.35 μm while keeping the same absorbed irradiance. This is consistent with the conclusion drawn from Fig. 12(a) on the predicted equality of m for spherical and for single-beam irradiation at $\lambda = 0.35$ μm. In other words, the unexpected experimental result[2] that m is as high at 1.05 μm as at 0.53 μm (for the same absorbed irradiance in spherical geometry) is attributed here to the nonlocal property of transport, which is greatly reduced at short wavelengths because of the higher collisionality. However, this result could also be attributed to significant absorption in the underdense plasma due to focusing much behind the target. Future experiments with short-wavelength irradiation in spherical geometry are expected to shed more light on this issue.

The importance of long-mean-free- path (mfp) electrons to the transport can be at the root of the difference found between single-beam and spherical experiments. In the former case, these long-mfp particles can be lost to the nonirradiated material surrounding the focal spot. Since they carry an insignificant fraction of the absorbed energy, x-ray imaging methods will show only little lateral heat transport. However, the loss of these particles results in the disappearance of the "foot" ahead of the heat front, without which the heat front can in fact be described by flux-inhibited transport. Therefore, *single-beam irradiation appears to indicate flux inhibition.*

This explanation is different than attributing the apparent flux inhibition in single-beam experiments to lateral heat transport. For example, the signature for lateral transport,[14] namely the much weaker dependence of m on I in single-beam as compared with spherical irradiation, does not appear in our 0.35 μm plane-target data [Fig. 12(a)]. However, these experiments still showed[3] flux inhibition. In other words, the amount of energy which flows laterally is small, which is consistent with only a small extension of x-ray images beyond the focal spot,[17] but nevertheless the flow of energy inwards is reduced. Forslund and Brackbill[18] attribute such reduction to magnetic-field-induced lateral convection of fast electrons. If this indeed is the correct explanation, one would measure flux inhibition even in focal spots whose radius is large enough for lateral heat transport to be negligible.

We show in Fig. 13 evidence that the same spectral features (hence, about the same temperature of the emitting region) indicate a higher density in uniform irradiation as compared with single-beam irradiation. The density dependence of the relative dielectronic satellite intensities is complex.[19] However, the intensity ratios in Fig. 13 indicate $N_e \gtrsim 4 \times 10^{22}$ cm^{-3} for the uniform case, and $N_e \lesssim 2 \times 10^{22}$ cm^{-3} for the single-beam case. The uniform-case density (at a given temperature contour on the heat front) is higher than that predicted by any flux-limited model. This again demonstrates the need to revise our current transport formulation.

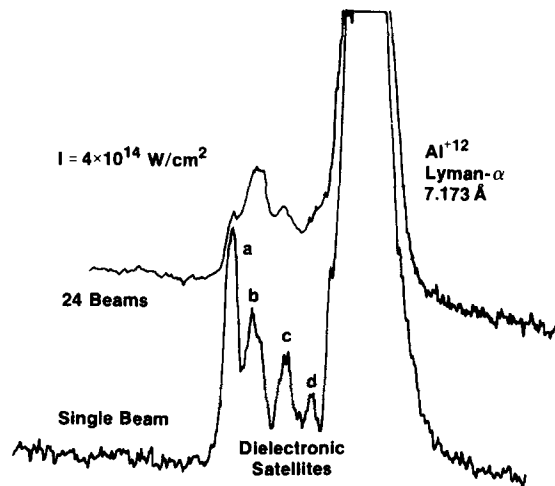The mass ablation rate is often used to deduce an abla-

FIG. 13. Dielectronic satellites indicating a higher density for the uniform irradiation case. Note the difference in intensity ratios of these lines.

tion pressure. The two are related in a simple way only when a steep temperature profile separates the accelerated material from the high pressure region (as in the rocket model). A reduced pressure gradient reduces the drive effectiveness (and the hydrodynamic efficiency). Therefore, the conclusion from Fig. 12(a) indicates that even though the ablation pressure for the same absorbed irradiance is wavelength independent, the *pressure gradient* should be higher for the shorter laser wavelength. This is *in addition* to the short-wavelength advantage of higher absorption for the same incident irradiance.

V. IMPLOSION EXPERIMENTS

Any modification in our modeling of transport should lead to modifications in the predicted core conditions at peak compression. Measuring these core conditions can, therefore, serve as a validity check of transport modeling. A variety of nonexplosive spherical implosions tend to show almost universally that *the core is considerably hotter than predicted by a flux-inhibited model* (incorporated into LILAC). "Nonexplosive" here simply means shells thicker than a typical range of preheating electrons or photons. For the irradiance values used here ($\leqslant 10^{15}$ W/cm^2) the range of electrons of average velocity produced by resonance absorption in parylene is smaller than 2 μm. Core conditions can also be determined by two-dimensional effects, but these results strongly suggest a more explosive implosion due to a penetrating temperature profile as the common denominator of all these experiments.

We show here one example of a hotter core than predicted by numerical simulation for an implosion experiment; as a target we chose an empty shell which was thick enough to be driven "ablatively" and of a low-enough aspect ratio ($\sim$40) to minimize instability effects. In the course of the implosion, the predicted aspect ratio increases slightly to about 50 before dropping rapidly. The target parameters are a glass shell of diameter 412 μm and thickness 0.9 μm, coated with a 0.25 μm thick aluminum layer and finally with a 4.1 μm thick parylene layer. The aluminum layer serves as a
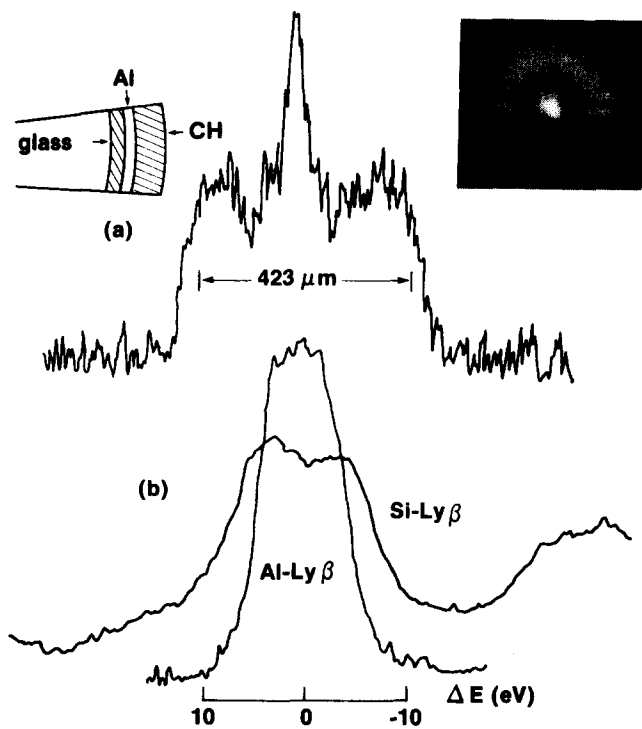
FIG. 14. The x-ray image (a) and a sample line spectra (b) from the implosion of a large (423 μm diameter) shell of low aspect ratio (40), at a peak irradiance of 4×10^{14} W/cm^2. Also shown in (a) is a linear scan through the pinhole camera image on the right-hand corner.

FIG. 15. Comparison of LILAC calculation of image scans for the shot of Fig. 14 for two values of the flux limiter f. The dashed line is the azimuthally averaged scan of the experimental image [Fig. 14(a)].

probe for parylene burnthrough (which is affected by the implosion of the shell). LILAC runs with either a flux limiter $f = 0.05$ or $f = 0.65$ predict an aluminum temperature much too low ($T \lesssim 50$ eV), throughout the implosion, to enable the observation of x-ray lines of either Al^{+11} or Al^{+12}. However, strong line emissions of both of these ions have been observed, indicating heat-front penetration into the aluminum layer. The code-predicted peak temperature of the inner glass surface at stagnation is barely sufficient for the emission of Si^{+12} lines, but is insufficient for the emission of Si^{+13} lines (it is about 0.25 keV for a run with $f = 0.05$ and 0.4 keV for a run with $f = 0.65$). Conversely, the experiment shows strong line emission of both Si^{+12} and Si^{+13} ions indicating $T > 0.6$ keV. This line emission could originate from the outer surface of the glass shell due to heat-front penetration. However, the broader Si lines, as compared with Al, indicate that Si^{+13} line emission probably originates primarily from the compressed core at the target center as we argue below. In Fig. 14 we show the profile of the Lyman-β line of Al^{+12} at 2.048 keV, broadened mostly due to the finite size of the target. The line profile of the same transition in Si^{+13} has the characteristic shape of a Stark profile, which indicates that the emission region of Si is much smaller than that of Al. Assuming that the source size contribution is negligible for the Si^{+13} Lyman-β line, we deduce through Stark profile fitting[20] a core electron density of 2×10^{23} cm^{-3}, or about 0.7 g cm^{-3}. This upper bound on the density is far smaller than that predicted by the one-dimensional code LILAC. The intensity of the observed lines was insufficient for high-resolution spectral imaging (using a slit). It should be noted, though, that the central emission seen in the inset of Fig. 14
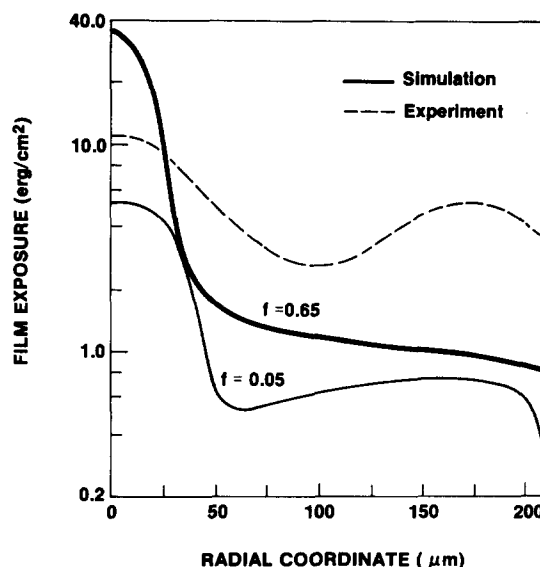
is entirely consistent with the assumption that it results from heating of the inner glass surface upon closure of this empty target.

Figure 14 also includes an x-ray pinhole camera image through a 6 μm Al filter, transmitting essentially the continuum around 1.2–1.5 keV. It shows a rather high degree of symmetry (poorly reproduced here) and the absence of shell breakup: the thick ring of radiation corresponds to the shell outer surface as it travels from its initial position to that at peak compression. We are, therefore, more confident in using the final core conditions as a signature of heat transport. Figure 15 compares this image with two LILAC-predicted images. The observed intensity of the ring is higher than predicted because of heat-front penetration into the aluminum layer. The higher intensity of the central spike, as compared with the $f = 0.05$ LILAC prediction, has to result from a hotter core in the experiments as compared with prediction (the density, as indicated above, is far lower). The higher central spike intensity when f is increased to 0.65 (no inhibition) is mostly due to an extremely high predicted density ($\gtrsim 100$ g cm^{-3}) which Si lines failed to show. We therefore conclude that the implosion must be more explosive (less ablative) than predicted by a flux-limited code simulation with either f value; measured core temperatures are higher and densities are lower than predicted. This is also indicated by the more diffuse profile of the central peak (Fig. 15) as compared with the code predictions. Implosion times could not be experimentally determined on these shots. Such measurements could substantiate this statement.

We finally cite results of another set of experiments[21] where the measured electron temperature of the compressed core was considerably higher than predicted by a flux-limited code: thin shells of diameter 400 μm filled with a mixture of 20 atm DT and 2 atm argon, were imploded with 1 nsec, 1.7 TW pulses (irradiance 10^{14} W/cm^2) on OMEGA. Here LILAC predicts an electron temperature around peak compression which ranges from about 0.5 keV at the center to

about 0.1 keV at the gas–glass interface. The spectroscopic measurements[21] of argon x-ray line emission indicate a temperature $\gtrsim 0.7$ keV throughout the fill gas.

VI. CONCLUSION

Transport and implosion experiments have been conducted on the OMEGA, 24-beam, uniform-irradiation facility that may result in significant revisions in our current understanding of thermal transport in laser-irradiated targets.

(a) Thermal transport in spherical irradiation could not be described in terms of a simple flux-limited inhibition model.

(b) Classical transport was found to be inadequate also: the heat front has a different shape (falling more gradually) than that predicted by either classical or flux-limited transport models for any level of inhibition.

(c) A multigroup (nonlocal) treatment of transport, in which faster than the average thermal electrons penetrate deeper, was found to result in a temperature profile which is in qualitative agreement with the present measurements.

(d) The enhanced inward penetration studied here appears to supercede preheat by resonance-absorption electrons, but to have a weaker dependence on the irradiance than is the case for the latter mechanism; this would reduce the incentive to go to lower irradiance in order to reduce preheat.

(e) Target implosion experiments showed higher core temperatures than predicted by an inhibited flux model and lower densities than predicted by an uninhibited flux model.

(f) Single-beam plane-target experiments appeared to show flux inhibition only because of some 2D effects; these may be subtler than simple lateral heat transport.

(g) There are indications that in short-wavelength irradiation the higher collisionality suppresses the deeper penetration measured here. This would mean that for the same absorbed irradiance the shorter-wavelength laser produces a higher pressure gradient (and efficiency).

Further experiments and analysis should be pursued to substantiate some of the tentative conclusions drawn here: (1) Mapping of the heat front by simultaneously measuring the density using various atomic species; (2) measuring the velocity and density of imploding shells under conditions similar to those used here; (3) computing and comparing with experiment the intensity and profile of the observed spectral lines of ionized species, using a rate-dependent model, in the context of a multigroup thermal transport model coupled to a hydrodynamic code; (4) similarly for K_α lines; and (5) determining whether apparent inhibition in single-beam irradiation persists even when the focal-spot diameter is much larger than the temperature gradient scalelength. If this be the case, magnetic fields probably play a dominant role in explaining the observations in single-beam irradiation.[20]

[1]C. E. Max, C. F. McKee, and W. C. Mead, Phys. Fluids **23**, 1620 (1980).

[2]T. J. Goldsack, J. D. Kilkenny, B. J. MacGowan, P. F. Cunningham, C. L. S. Lewis, M. H. Key, and P. T. Rumsby, Phys. Fluids **25**, 1634 (1982).

[3]F. C. Young, R. R. Whitlock, R. Decoste, B. H. Ripin, D. J. Nagel, J. A. Stamper, J. M. McMahon, and S. E. Bodner, Appl. Phys. Lett. **30**, 45 (9177); B. Yaakobi, T. Boehly, P. Bourke, Y. Conturie, R. S. Craxton, J. Delettrez, J. M. Forsyth, R. D. Frankel, L. M. Goldman, R. L. McCrory, M. C. Richardson, W. Seka, D. Shvarts, and J. M. Soures, Opt. Comm. **39**, 175 (1981).

[4]R. C. Malone, R. L. McCrory, and R. L. Morse, Phys. Rev. Lett. **34**, 721 (1975).

[5]M. D. Rosen, D. W. Phillion, V. C. Rupert, W. C. Mead, W. L. Kruer, J. J. Thompson, H. N. Korublum, V. W. Slivinsky, G. J. Caporaso, M. J. Boyle, and K. G. Tirsell, Phys. Fluids **22**, 2020 (1979).

[6]R. Fabbro, E. Fabre, F. Amiranoff, C. Garban-Labaune, J. Virmont, M. Weinfeld, and C. E. Max, Phys. Rev. A **26**, 2289 (1982).

[7]Crystals calibrated by A. J. Burek, National Bureau of Standards, Gaithersburg, MD 20760. Our film calibration results agree (except for very high exposures) with published data: R. F. Benjamin, P. B. Lyons, and R. H. Day, Appl. Opt. **16**, 393 (1977); and C. M. Dozier, D. B. Brown, L. S. Birks, P. B. Lyons, and R. F. Benjamin, J. Appl. Phys. **47**, 3732 (1976).

[8]Earlier versions of LILAC are described in Laboratory for Laser Energetics Reports No. 16, 1973 and No. 36, 1976; opacity tables from W. F. Huebner, A. L. Merts, N. H. Magee, and M. F. Argo, Los Alamos Report No. LA-6760, 1977.

[9]The energy fraction which reaches the critical surface by tunneling and is converted to fast electrons is calculated by W. L. Kruer, Lawrence Livermore Laboratory Report UCRL-81896, 1978; see also K. Estabrook and W. L. Kruer, Phys. Rev. Lett. **40**, 42 (1978).

[10]D. Shvarts, J. Delettrez, R. L. McCrory, and C. P. Verdon, Phys. Rev. Lett. **47**, 247 (1981).

[11]A. R. Bell, R. G. Evans, and D. J. Nicholas, Phys. Rev. Lett. **46**, 247 (1981).

[12]B. Yaakobi, J. Delettrez, L. M. Goldman, R. L. McCrory, W. Seka, and J. M. Soures, Opt. Comm. **41**, 355 (1982).

[13]Lawrence Livermore National Laboratory Report UCRL-50021-79, 1980, edited by L. W. Coleman and W. F. Krupke, Vol. 2, pp. 6–23 (unpublished).

[14]M. H. Key, W. T. Toner, T. J. Goldsack, J. D. Kilkenny, S. A. Veats, P. F. Cunningham, and C. L. S. Lewis, Phys. Fluids **26**, 2011 (1983).

[15]R. J. Mason, Phys. Rev. Lett. **47**, 652 (1981).

[16]D. Shvarts, J. Delettrez, and R. L. McCrory (to be submitted for publication).

[17]J. Murdoch, J. D. Kilkenny, D. R. Gray, and W. T. Toner, Phys. Fluids **24**, 2107 (1981).

[18]D. W. Forslund and J. U. Brackbill, Phys. Rev. Lett. **48**, 1614 (1982).

[19]J. G. Lunney and J. F. Seely, J. Phys. B **15**, L121 (1982).

[20]P. C. Kepple and H. R. Griem (private communication).

[21]B. Yaakobi, D. M. Villeneuve, M. C. Richardson, J. M. Soures, R. Hutchinson, and S. Letzring, Opt. Comm. **43**, 343 (1982).

526   Phys. Fluids, Vol. 27, No. 2, February 1984

Yaakobi *et al.*   526